Soft Matter



PAPER



Cite this: Soft Matter, 2021. **17**, 9745

Received 6th April 2021, Accepted 14th September 2021

DOI: 10.1039/d1sm00517k

rsc.li/soft-matter-journal

Instabilities and patterns in a submerged jelling iet†

Aditi Chakrabarti, 🕩 ‡ a Salem Al-Mosleh 🕩 ‡ and L. Mahadevan 🕩 *abc

When a thin stream of aqueous sodium alginate is extruded into a reacting calcium chloride bath, it polymerizes into a soft elastic tube that spontaneously forms helical coils due to the ambient fluid drag. We quantify the onset of this drag-induced instability and its nonlinear evolution using experiments, and explain the results using a combination of scaling, theory and simulations. By co-extruding a second (internal) liquid within the aqueous sodium alginate jet and varying the diameter of the jet and the rates of the co-extrusion of the two liquids, we show that we can tune the local composition of the composite filament and the nature of the ensuing instabilities to create soft filaments of variable relative buoyancy, shape and mechanical properties. Altogether, by harnessing the fundamental varicose (jetting) and sinuous (buckling) instabilities associated with the extrusion of a submerged jelling filament, we show that it is possible to print complex three-dimensional filamentous structures in an ambient fluid.

Slender filamentous structures buckle, fold and coil on a range of length scales spanning the nanometric to the macrometric. For example, an elastic rope fed uniformly toward a horizontal plane coils into a spool;¹⁻³ similar behavior is seen in a slender jet of viscous fluid.⁴⁻⁷ In both cases, the presence of the plane boundary leads to compressive stresses, while geometric scale separation implies the dominance of bending deformations. Quantitative predictions for the coiling rates and radii then arise from the balance of internal elastic or viscous forces and inertia and/or gravity. The patterns arising from these instabilities have also been harnessed to fabricate structures by coupling them to phase changes in solidifying polymers and glass.⁸⁻¹⁰ Here, partly inspired by these examples, and partly by

the quest to pattern filaments in three dimensions without a sacrificial scaffold as exemplified by the 3Doodler pen, 11 we ask if there are instabilities and patterns that can be harnessed when a filament moves through an ambient fluid while also changing from a liquid to solid. An example of this can be seen in high speed liquid polymer extrusion in air, 12 where solventloss driven solidification happens so fast that it is almost impossible to control the instability. But could one extrude a viscous filament in an aqueous bath containing a crosslinker that causes the stream to polymerize, buckle and coil due to the resisting viscous drag forces from the surrounding medium, even in the absence of compressive stresses due to a solid boundary? And then control the patterns by varying the extrusion

^a John A. Paulson School of Engineering and Applied Sciences, Harvard University, Cambridge, MA 02138, USA. E-mail: lmahadev@g.harvard.edu

^b Department of Physics, Harvard University, Cambridge, MA 02138, USA

^c Department of Organismic and Evolutionary Biology, Harvard University, Cambridge, MA 02138, USA

[†] Electronic supplementary information (ESI) available: Movie S1: Viscous drag induced instability of an extruded polymerizing jet of 2% sodium alginate (Q₀ = 2 ml min⁻¹ and needle diameter d = 0.41 mm) entering in a water bath containing 150 mM calcium chloride salt. Movie S2: Four regimes of instability of the submerged jelling jet of 2% sodium alginate in a 150 mM calcium aqueous bath, namely: (i) gravity driven coiling (needle diameter d = 0.84 mm, extrusion rate Q₀ = 0.5 ml min⁻¹), (ii) drag induced coiling (needle diameter d = 0.84 mm, $Q_0 = 5 \text{ ml min}^{-1}$), (iii) period doubling (needle diameter d = 0.6 mm, $Q_0 = 5 \text{ ml min}^{-1}$) and (iv) chaotic crumpling (needle diameter d = 0.6 mm, $Q_0 = 15 \text{ ml min}^{-1}$). Snapshots of these four regimes and the phase space are shown in Fig. 1B. Movie S3: Four videos (1× speed) showing the chaotic crumpling of the submerged jelling jet of 2% sodium alginate in a 150 mM calcium aqueous bath for a fixed needle size (d = 0.16 mm) and increasing extrusion rate $Q_0 = 8, 10, 15, 20 \text{ ml min}^{-1}$. Snapshots of the chaotic crumpling and characterization of their plume angles are shown in Fig. 4. Movie S4: Results from the 3D simulation of injected elastic threads: (A) classical gravity induced rope coiling with vanishing drag. Parameters used are: $\nu = 1$ cm s⁻¹, d = 1.5 mm, linear density $\rho_{\rm L} = 2.9~{\rm kg~m}^{-1}$, $E = 8.5~{\rm MPa}$ and $\ell_{\rm g} \equiv (Er^2/\rho g)^{1/3}$. The resulting radius of coiling is consistent with the experiments done in ref. 2. (B) Long time behavior of drag induced coiling without crosslinking and hydrodynamic interactions. The coils at the free end unwind. Parameters used: E = 4.8 kPa, $Q = 10 \text{ ml min}^{-1}$, d = 1 mm, $\Delta \rho = 15 \text{ kg m}^{-3}$ and $\mu = 0.001$ Pa s. (C) Adding crosslinking and hydrodynamic interactions, we get regular stacks of coils. After reaching a steady state, vertices are removed from the free end to speed up the simulation. Parameters used: E = 2.7 kPa, Q = 1 ml min⁻¹, d = 0.8 mm, $\Delta \rho = 5$ kg m⁻³ and $\mu = 0.01$ Pa s. Movie S5: Controlled patterning of the co-extruded jet with outer sodium alginate $(Q_0 = 20 \text{ ml min}^{-1})$ and inner red dyed silicone oil $(Q_i = 10 \text{ ml min}^{-1})$ entering an aqueous calcium bath. The size of the inclusions is selected due to the pinch-off instability of the internal oil jet. The alginate and oil meet at a T-junction before entering the calcium aqueous bath through a common needle tip, with the outer alginate needle (15G, d = 1.4 mm) and oil needle (18G, d = 0.84 mm). The resulting composite tube is buoyant and floats up at the interface of the air-aqueous calcium bath. See DOI: 10.1039/d1sm00517k

[‡] These authors contributed equally to this work.

Paper Soft Matter

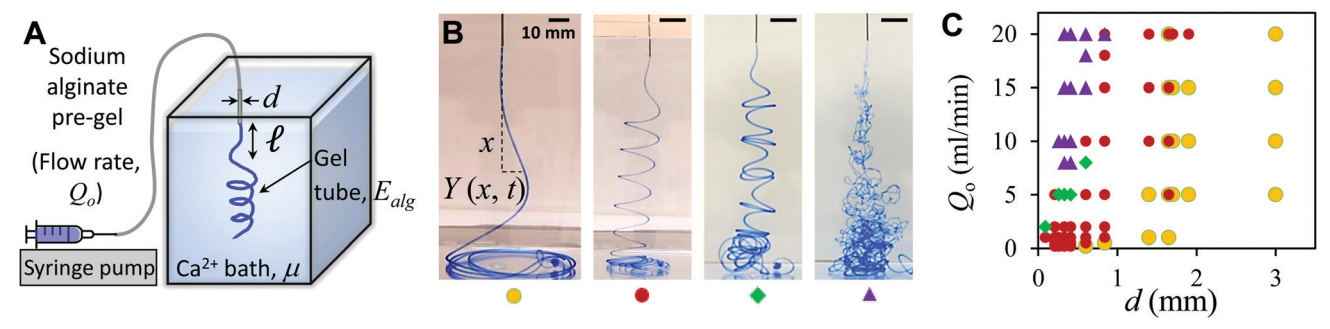


Fig. 1 Instability of a submerged jelling jet. (A) Schematic of the experimental setup that is used to obtain the drag induced coiling instability of a solidifying sodium alginate gel tube in a water bath containing 150 mM calcium chloride. A syringe pump is used to deliver the 2% sodium alginate solution, dyed with methylene blue, at a prescribed flow rate (Q_o) via a blunt-tipped needle (inner diameter, d) into the calcium bath. As the sodium alginate solution contacts the calcium ions in the water bath, it begins to crosslink to form an elastic soft tube and then buckles due to the compression induced by the viscous drag of the surrounding liquid. (B) As the flow rate Q_o is increased, we see a transition from classical rope coiling (yellow circles, 18G needle, d = 0.84 mm at $Q_o = 0.5$ ml min⁻¹), to drag-induced elastic coiling (red circles, 22G needle, d = 0.41 mm at $Q_o = 0.5$ ml min⁻¹), to chaotic crumpling (purple triangles, 22G needle, d = 0.41 mm at $Q_o = 0.05$ ml min⁻¹) (see Movie S2, ESI†). All scale bars are 10 mm. (C) Phase space of the instability regimes shown in (B) plotted as a function of the flow rates of the alginate extrudate Q_o and the needle inner diameters d.

rate and even the properties by co-extruding a second fluid within the jelling jet?

We answer both questions in the affirmative. By extruding an alginate solution into a calcium bath, we study the onset of a periodic coiling instability as well as its saturation *via* a combination of scaling analysis, stability theory and computation. By introducing a second fluid at the inlet, we show that we can add periodic droplet inclusions of oil and gas to the soft filaments. This allows for a single-step fabrication protocol to make a continuous soft filament of varying composition, stiffness, curvature and buoyancy that can be used to write and draw patterns in 3 dimensions in an ambient fluid without a sacrificial substrate.

Experimental observations

Our experimental setup (Fig. 1A) for the fabrication of single phase gel filaments and tubes uses a 2% w/w sodium alginate solution, dyed with 0.01% w/w methylene blue, filled in plastic syringes, and dispensed inside an aqueous bath (viscosity μ) of calcium chloride salt (150 mM in water) at extrusion rates $(Q_0, 0.1-20 \text{ ml min}^{-1})$ via needles (inner diameter d, 0.1-2 mm) (see Appendix A.1 and Movie S1 for more details, ESI†). For all the experiments, the concentrations of sodium alginate and calcium chloride in the respective aqueous solutions were kept fixed, thereby fixing the reaction rate (k) of gelation. As the polymerization progresses,13 the elastic Young's modulus of the crosslinked alginate tubes increases from hundreds of pascals (within a few seconds) to tens of kilopascals (over several minutes). We quantify this change in the stiffness via simple gravity-driven bending of filament segments, removed at different times from the calcium chloride solution (Appendix A.2 and Fig. 8A, B).

For extrusion from a given needle diameter (d) at very low flow rates (Q_0) , a thin stream of alginate extruding inside the calcium bath polymerizes to form an elastic tube. In this

regime, when the elastic tube pushes against the base of the container, it starts to coil like an elastic rope^{1,2} (Fig. 1B, first panel), due to the resulting compressive stresses induced in the filament. However, as Q_0 is increased, the polymerized elastic tube begins to buckle over a characteristic length ℓ much smaller than the falling height, and spontaneously forms loosely coiled helices (radius, R, and vertical spacing between coils, Λ) as it falls through the liquid bath (Fig. 1B, second panel and Appendix, Fig. 6). In this regime, there is no influence of the floor. Further increase in the extrusion rate Q_0 leads to more complex patterns that exhibit signs of period doubling in the spacing between the helical coils (Fig. 1B, third panel), and when Q_0 is very large, the jet polymerizes and crumples chaotically forming rough tubes that stay within a conical region (Fig. 1B, last panel, Appendix, Movies S2 and S3, ESI†). The phase space of patterns and morphologies are determined by the extrusion rate (Q_0) and the needle diameter (d) as shown in Fig. 1C (Movie S2, ESI†).

Scaling analysis and stability theory

To understand these patterns, we note that if the polymerization process with a rate k is relatively fast, *i.e.* $kd/v \gg 1$ (v is the speed of extrusion and d the diameter of the needle which is comparable to the diameter of the tube, 2r, that forms), the polymerized filament behaves like an elastic filament of bending stiffness B. If the filament buckles over a characteristic scale ℓ , we can balance the resisting bending torque B/ℓ in the filament with the forcing viscous torque from the ambient fluid that scales as $\mu v \ell^2$ to find a characteristic length scale^{14,15}

$$\ell \sim \left(\frac{B}{\mu v}\right)^{1/3},\tag{1}$$

above which the extrudate should buckle and coil into a helix spontaneously. Beyond the onset of buckling, we expect the radius of the helical coil to follow this same scaling with $R \sim \ell$, while the

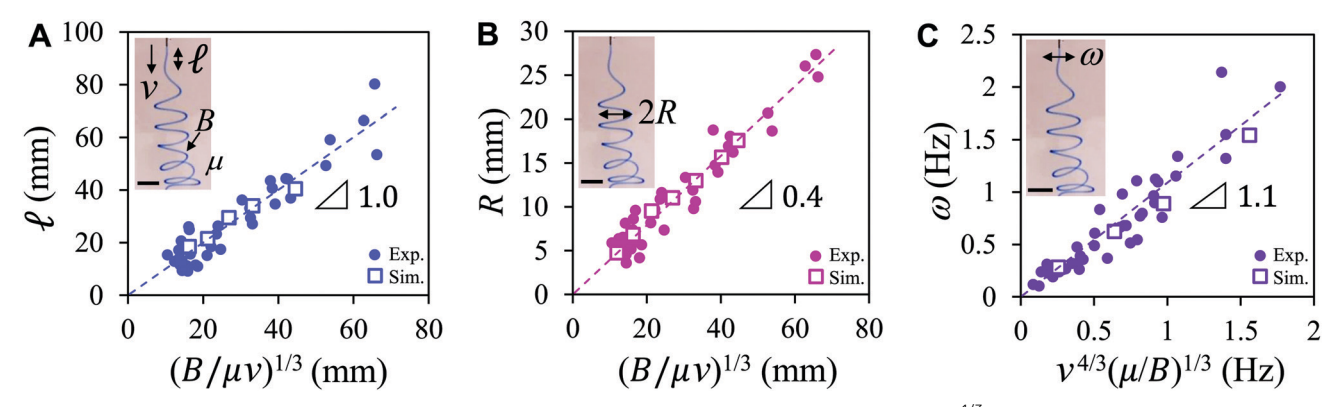


Fig. 2 Understanding the instability. (A) The measured buckling length ℓ is plotted as a function of $(B/\mu v)^{1/3}$ for various experiments (closed circles), where needle diameters d varied from 0.1 mm to 2 mm, and flow rates varied from 0.2 ml min⁻¹ to 20 ml min⁻¹. Simulation data are shown with open square symbols. (inset) Experimental snapshot to define ℓ , extrusion velocity ν , viscosity of bath μ and bending stiffness B of the polymerized filament. (B) Characterization of the drag induced elastic coiling instability in term of the coiling radius (R) plotted as a function of the scaling relationship $(B/\mu\nu)^{1/3}$, with a slope of 0.4 for the linear regression for both experiments and simulation. (inset) Definition of coiling radius R. (C) The frequency of coiling ω for the experimental and simulation data shows that it scales as $v^{4/3}(\mu/B)^{1/3}$ with a slope of 1.1. (inset) Definition of ω . Scale bars in insets in (A–C) are 5 mm each.

frequency of coiling is expected to behave as

$$\omega \sim v/\ell \sim v^{4/3} \left(\frac{\mu}{B}\right)^{1/3}.$$
 (2)

Plotting the experimental data for buckling length ℓ , coiling radius R and coiling frequency ω (Fig. 2), we find that the data agree well with the scaling expressions obtained above. The vertical spacing between the coils (Λ) also remain steady while the stack of freshly coiled alginate tubes descends through the ambient calcium solution (Fig. 6 and Movie S1, ESI†). Furthermore, we see that the entire range of scenarios from gravity-induced to drag-induced elastic coiling can be collapsed to a single universal scaling law that interpolates between two limits, gravity-induced coiling and drag-induced coiling, leading to an expression

$$\ell \sim (B/(\mu v + \Delta \rho g r^2))^{1/3} \tag{3}$$

where $\Delta \rho$ is the density difference between the alginate tubes and the surrounding calcium bath (Fig. 3). In the limit of no external fluid, we recover the well-known scaling law for elastic folding and coiling^{1,16} $\ell_{g} \sim (B/\rho gr^{2})^{1/3}$.

Moving beyond a scaling analysis, we consider the linear stability of a thin elastic rod with length L, moving in a fluid with viscosity μ at a speed ν , in the limit of low Reynolds number, i.e. $\rho v L/\mu \ll 1$. For a flexible rod whose center line follows a path Y(x, t) (see Fig. 1B) that is only slightly deviated from being straight, force balance in the tangential and normal directions yields

$$0 = \nu \mu_{\rm s} + \partial_x T(x, t), \tag{4}$$

$$0 = 2\mu_{\mathrm{s}}\partial_{t}Y(x, t) + \nu\mu_{\mathrm{s}}\partial_{x}Y(x, t) + B\partial_{x}^{4}Y(x, t) - \partial_{x}(T(x, t)\partial_{x}Y(x, t)).$$

$$(5)$$

Here T(x, t) is the tension in the rod, and μ_s and $2\mu_s$ are the effective drag coefficients in the tangential and normal directions ($\mu_s \sim \mu$, up to logarithmic factors in the aspect ratio) obtained from slender body theory.17 The accompanying boundary conditions are that at the free end x = 0, $\partial_x^2 Y(0, t) =$ $\partial_x^3 Y(0, t) = T(0, t) = 0$ while at the needle x = L = vt, the clamped boundary conditions read $Y(L, t) = \partial_x Y(L, t) = 0$.

Solving eqn (4) to get $T = -\mu_s vx$ and substituting the result into eqn (5) while using the ansatz $Y(x, t) = \eta(x)e^{\sigma t}$ to determine

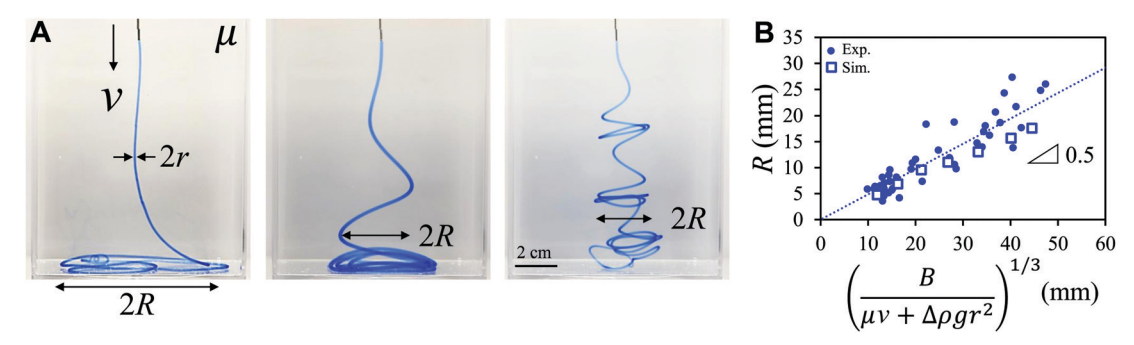


Fig. 3 Generalized scaling law to unify gravity induced and drag-induced coiling. (A) Pictures showing the gravity driven classical rope coiling (left: 18G needle, d = 0.84 mm at $Q_0 = 0.5$ ml min⁻¹), drag-induced elastic coiling (centre: 18G needle, d = 0.84 mm at $Q_0 = 5$ ml min⁻¹) and period doubling (right: 20G needle, d = 0.6 mm at $Q_0 = 5 \text{ ml min}^{-1}$) (see Movie S2, ESI†). (B) Radius of coil as a function of $[B/(\mu v + \Delta \rho g r^2)]^{1/3}$ shows the experimental data over the regime of gravity-driven coiling and drag-induced coiling, with a slope of 0.5. The simulation data is seen to match the experimental data.

Paper Soft Matter

the growth rate of an instability σ yields the eigenvalue problem

$$2\mu_{s}\sigma\eta(x) + 2\nu\mu_{s}\eta'(x) + B\eta''''(x) + \mu_{s}\nu x\eta''(x) = 0.$$
 (6)

Since $\eta \to -\eta$ is a symmetry of the equation for real solutions $\eta(x)$, the growth rate σ will also be real. At the onset of instability Re[σ] = σ = 0 so that eqn (6) can be rewritten in scaled form as

$$2\eta'(\xi) + \beta^{-1}\eta^{(4)}(\xi) + \xi\eta''(\xi) = 0, \tag{7}$$

where $x = L\xi$ and $\beta \equiv \mu_s v L^3/B$. By using the boundary conditions at the free end, the solution to this equation can be written as

$$\eta(\xi) = A + C\xi_0 F_1 \left(\frac{4}{3}; -\frac{\xi^3 \beta}{9}\right),$$
(8)

where ${}_0F_1$ is the confluent hypergeometric function. ¹⁸ Using the boundary condition at the extruding end $\eta(1) = 0$, $\eta'(1) = 0$ then yields

$$_{0}F_{1}\left(\frac{4}{3}; -\frac{\beta}{9}\right) = \frac{\beta}{4} {_{0}F_{1}\left(\frac{7}{3}; -\frac{\beta}{9}\right)},$$
 (9)

a condition only satisfied for special values of β . Solving (9) numerically we find that this first happens for $\beta \approx 3.48$ and thus yields

$$\ell \approx 1.41 \left(\frac{B}{\mu v}\right)^{1/3}.\tag{10}$$

The above equation also yields an expression for the oscillation frequency $\omega_{\rm c} \equiv \nu/\ell \approx 0.71 \nu^{4/3} (\mu/B)^{1/3}$. Numerical simulations (described in Appendix A.3) confirm this result; filaments with lengths just above the threshold given in eqn (10) buckle, while shorter ones do not.

Using experimental parameter values in the range $B \sim Er^4$ (E = 2.7 kPa, $r \sim 0.1$ –2 mm), $\mu \sim 0.001$ Pa s and $\nu \sim 2$ –70 mm s⁻¹, the experimentally obtained relation for the buckling length is $\ell \sim 1.04 (B/\mu v)^{1/3}$ (Fig. 2A and B) while that for the frequency is $\omega \sim 1.1 \nu^{4/3} (\mu/B)^{1/3}$ (Fig. 2C), in reasonable agreement with the values obtained from the calculation above.

Multiscale control of filament structure and morphology

We can use our understanding of the drag-induced coiling instability to control filament curvature. Since coiling is induced by an ambient drag, if polymerization occurs slowly, filament curvature can get frozen due to polymerization being a function of the scaled polymerization rate kd/v (here k is the polymerization rate, and $v = Q_0/d^2$ is the flow velocity). At low flow rates, the tubes are relatively straight, while at higher flow rates, the tubes are strongly crumpled within an approximately conical plume (Fig. 4A), with an opening angle θ that varies linearly with needle diameter (Fig. 4B and Movie S3, ESI†). In this strongly crumpled regime, the polymerized tubes have a disordered morphology driven by the coupled dynamics of flow and polymerization that occur on similar time scales. The morphology can be quantified in terms of the variance of the curvature of the center line of these tubes as a function of the flow rate Q_0 (Fig. 4C). Turning this bug into a feature suggests a method to fabricate filaments of varying the curvature by controlling the needle diameter and the extrusion rate to 'freeze' the dynamic instability of the filament. Conversely, in this chaotic crumpling regime, the small scale roughness in the filaments (Appendix, Fig. 9) could also serve as a read out of the interfacial shear instability¹⁹ between the viscoelastic sodium alginate jet and the Newtonian fluid aqueous calcium chloride bath.

In addition to controlling the global morphology of the filament, we can also control its local structure and properties such as its buoyancy, rigidity, and curvature. To do so, we introduce a second fluid such as an oil (e.g. silicone oil, $\rho_{\rm oil} \sim 972~{\rm kg~m^{-3}}$), or a gas (e.g. compressed nitrogen) that is internally co-extruded with the alginate solution, as shown schematically in Fig. 5A (Movie S5, ESI†). At low co-extrusion rates, the internal fluid pinches off due to interfacial forces, and forms small droplet inclusions. By varying the relative flow rates of the co-extruding fluid (Q_i) and the encasing alginate (Q_o), we can control the size, spacing and position of the fluid

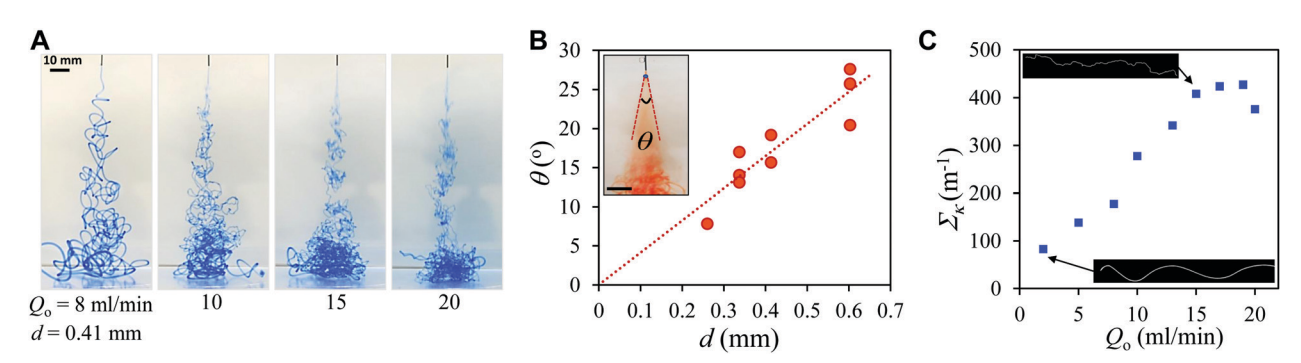


Fig. 4 Characterization of the chaotic plume. (A) Snapshots of the chaotic plume observed for high flow rates (Q_o) (22G needle, d=0.41 mm) (see Movie S3, ESI†). (B) The plume angle (θ) of the gel tubes in the chaotic regime for different inlet needle diameters (d) and extrusion rates (Q_o) . θ increases linearly with needle diameter (d), and is weakly dependent on Q_o (depicted by the vertical spread at a given value of d and in A). Inset shows an example image of the plume shape, associated with a 22G needle (d=0.41 mm) at $Q_o=15 \text{ ml min}^{-1}$, where θ is measured from the point where the plume opens. Scale bar is 10 mm. (C) Characterization of the chaotic regime using the standard deviation of curvature (Σ_κ) of the gel tubes formed at high extrusion rates (22G needle, d=0.41 mm). As Q_o increases, Σ_κ increases and then saturates at very high rates due to the finite thickness of the tubes.

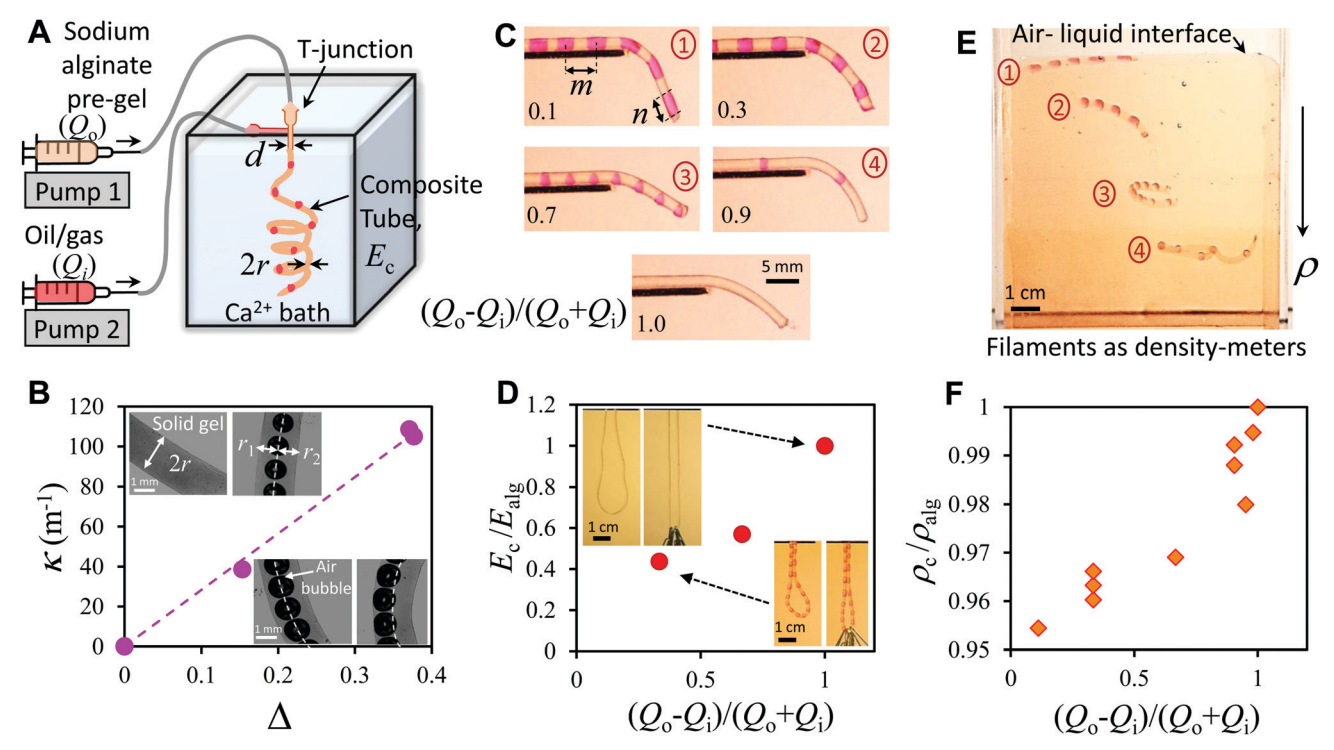


Fig. 5 Controlled patterning of co-extruded jelling jet. (A) Schematic of the experimental setup used to obtain composite fluid-in-solid tubes via polymerization of co-extruding two liquids (2% sodium alginate, Qo and inner fluid, Qo) into an aqueous bath containing 150 mM calcium chloride (needle inner diameter, d). A T-junction in the tubing allows the alginate solution and embedded fluid to meet, before entering the calcium bath. (B) Tube shape can be controlled by the inclusion of air bubbles at a prescribed (mis)alignment with the central axis of the tube, quantified by $\Delta = (r_1 - r_2)/r$, which dictates composite tube curvature (κ). (C and D) Controlling elastic moduli with inclusions: (C) gravity driven bending of small segments of composite filaments show that elastic moduli of filaments vary when oil droplets (silicone oil, kinematic viscosity \sim 100 cSt, $\rho_{\rm oil}$ = 972 kg m⁻³, flow rate Q_i , dyed red) are co-extruded within the alginate (outer extrusion rate, Q_o). Varying the relative flow rates of oil and alginate ($Q_o - Q_i$)/($Q_o + Q_i$) controls filament morphology (spacing between oil inclusions, m and the size of the inclusions, n) and thence the elastic moduli. (D) The normalized elastic moduli of the composite tubes (E_c/E_{alo}) can be measured by stretching the tubes (inset) and plotting the normalized ratio E_c/E_{alo} as a function of $(Q_o - Q_i)/(Q_o + Q_i)$. (E and F) Controlling density with inclusions: (E) the density of alginate tubes (pure, $\rho_{alg} = 1054$ kg m⁻³) can be lowered by introducing oil inclusions $(\rho_{\text{cil}} = 972 \text{ kg m}^{-3})$ to form composite tubes $(\rho_{\text{c.}}, (1) 1006 \text{ kg m}^{-3}; (2) 1018 \text{ kg m}^{-3}; (3) 1021 \text{ kg m}^{-3};$ and (4) 1045 kg m⁻³). Suspending these filaments in a density gradient allows for a direct readout of the density (ρ_c) of the column as the filaments become neutrally buoyant at a height where filament and liquid densities are matched. Here, the density at the bottom of the container is 1050 kg m^{-3} and at the air liquid interface is 1010 kg m^{-3} . (F) The normalized density of the composite tubes (ρ_c/ρ_{alq}) are plotted as a function of $(Q_o - Q_i)/(Q_o + Q_i)$.

droplet inclusions in the gel filaments. By (mis)aligning the gas bubbles relative to the axis of the filament (Fig. 5B), we can control filament curvature. By varying the fraction of internal droplets of oil or gas, we can also control the effective filament bending and stretching stiffness (Fig. 5C, D and Appendix, Fig. 8C, D) as well as the filament density and buoyancy (Fig. 5E and F). Altogether, this allows us then to print and write out stable structures in the ambient liquid by dynamically varying the co-extrusion rate of the internal fluid (oil/gas) and the extrusion of the alginate, as seen in Fig. 5.

Conclusions

Complementing the study of fluid filament coiling driven by boundary compression seen in the familiar honey-on-toast experiment, here we have examined the coiling of a submerged jelling jet driven by bulk drag. A combination of experimental observations, scaling analysis, stability theory and simulations

allowed us to characterize the onset and the nonlinear evolution of periodic coiling. We then explored the possibility of controlling this instability to create complex structures. By harnessing the simplest instabilities in elastic filaments and fluid jets, namely the buckling of a slender elastic filament and the breakup of a slender liquid jet, we showed how to create a quasi-one dimensional liquid-solid composite. The co-extrusion of a thin stream of aqueous sodium alginate and a second liquid into a reacting calcium chloride bath leads to the pinch off of the internal liquid to form a beaded filament that buckles and coils. By controlling the relative rates of polymerization of the sodium alginate, with calcium ion concentration, and the mechanical instability of the freshly formed filaments, we demonstrated the use of the underlying dynamical processes to write in three dimensions while controlling filament properties such as buoyancy, stiffness, curvature and chirality. Our ability to control and steer the shape of the soft filaments using an instability complements the deterministic approach used to deposit each voxel in the additive manufacturing process²⁰ and suggests alternative ways

to manufacture and engineer low-dimensional fluid-solid composites^{21–23} for various applications.^{24,25}

Conflicts of interest

There are no conflicts to declare.

Appendix

A.1 Materials

The pre-gel alginate solution was prepared by dissolving 2% by weight (w/w) sodium alginate (Sigma Aldrich) in freshly collected deionized (DI) water, to which, 0.01% weight (w/w) of methylene blue dye (Sigma Aldrich) was added to aid visualization. The aqueous calcium bath was prepared by dissolving 150 mM of calcium chloride salt in DI water (i.e., 17 g of CaCl₂ hexahydrate, Sigma Aldrich, in 1000 g water), which were filled in clear plastic containers (10 cm \times 10 cm \times 12.5 cm height). The dynamic viscosity μ of calcium bath was 0.001 Pa s. Direct measurement of densities (ρ) gave 1054 kg m⁻³ for 2% sodium alginate and 1051 kg m⁻³ for 150 mM calcium chloride solution, and these concentrations of solutions were specifically chosen such that sodium alginate was marginally denser than the calcium bath. The 2% sodium alginate solution was filled in plastic syringes, delivered via a syringe pump and dispensed inside the calcium bath via blunt-tip needles (32G to 12G, inner diameter, $d \sim 0.09$ –1.9 mm respectively). The extrusion flow rates Q_0 of the alginate solution was varied between 0.1 ml min⁻¹ and 20 ml min⁻¹. We used new needles for each experiment as it was crucial to maintain a clean unclogged tip. In each experiment, the calcium bath was stirred to maintain homogeneous ion concentration. The calcium bath was replaced by fresh solution after approximately ten experiments. The radius of the gelled tubes are linearly proportional to the needle radii and weakly depend on the inlet extrusion

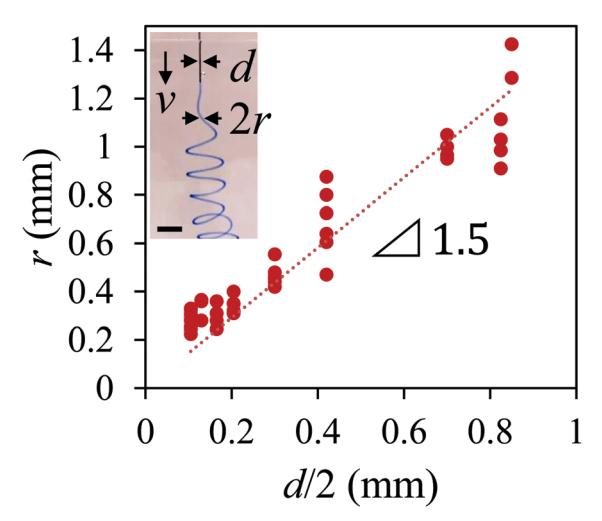


Fig. 7 Experimental characterization of filament radius r as a function of needle inner radius d/2. The vertical spread at each value of d/2 is due to extrusion velocity v, varying between 1–15 ml min⁻¹. Scale bar is 5 mm.

rate (Fig. 7). For the multiphase composite tubes, embedding fluids such as silicone oil (density, $\rho_{\text{oil}} = 972 \text{ kg m}^{-3}$, kinematic viscosity, 100 cSt) with red dye (silcPig) and compressed nitrogen gas were injected at a flow rate of Q_i (Fig. 5A). By controlling relative rates of Qo and Qi, various properties (buoyancy, curvature, and stiffness) of the resulting composite fluid-insolid filaments were controlled. All the experiments were performed at room temperature of 23 °C. For thicker needles (15G-12G, inner diameters, $d \sim 1.4$ -1.9 mm respectively) a 25 L plastic tank (41 cm \times 28 cm \times 30 cm height) was used for the experimental measurements of the coiling instability.

A.2 Experimental methods

A.2.1 Elastic moduli of the polymerized composite tubes. The elastic modulus of the extruded polymerized tubes and

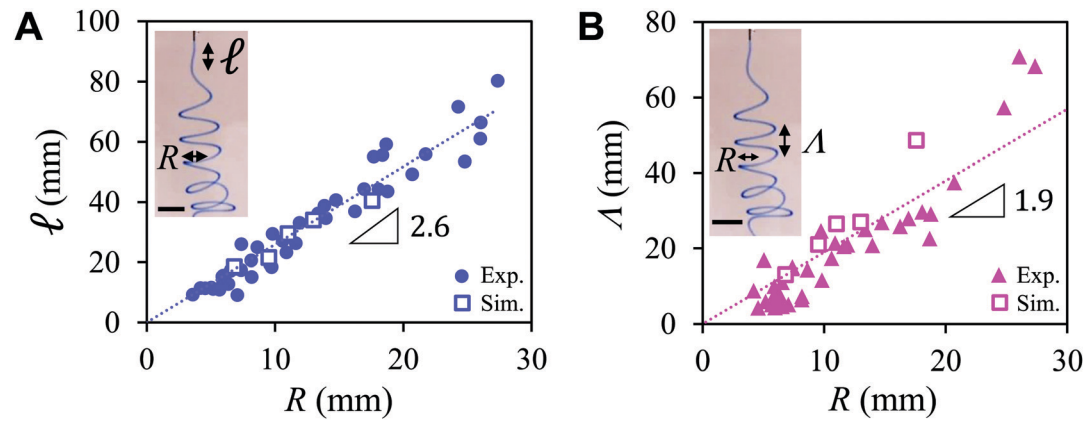


Fig. 6 Characterization of buckling length and vertical spacing in the drag-induced coiling instability. (A) The directly measured buckling length / is plotted as a function of the coiling radius R across various experiments, where needle diameters d varied from 0.1 mm to 2 mm, and flow rates varied from 0.2 ml min^{-1} to 20 ml min^{-1} . ℓ shows an expected linear correlation with R with a slope of 2.6. Simulations agree well with the experimental data. (inset) Experimental snapshot to define ℓ and R. (B) Measurement of vertical spacing between adjacent coils Λ of a crosslinked tube during the descent of the coiled helices in the calcium bath during the drag induced instability, as a function of R for both experiments and simulations. (inset) Experimental snapshot to define Λ and R. Scale bar in both insets is 5 mm.

filaments were measured by bending experiments of the filaments. Small segments ($\sim 1-2$ cm) of the polymerized filaments were mounted such that its one edge was on a horizontal substrate. The other end was suspended such that gravity could weigh it down. The downward displacement (δ) as a function of the overhung length of the filament from the edge (λ) were measured (Appendix, Fig. 8). A simple calculation using Euler-Bernoulli beam theory gives the solution for the bending profile of the elastic filament due to a distributed load q (force per unit length). In particular, we get

$$\delta = \frac{q\lambda^4}{8EI}, \quad I = \frac{\pi r^4}{4}, \quad q \equiv \pi r^2 \rho g \Rightarrow \lambda^4 = \frac{2Er^2}{\rho g}\delta.$$
 (A.1)

Using the slope of the plot of λ^4 vs. δ for freshly crosslinked alginate tubes extracted from solution close to the needle tip (seconds after it has formed, Appendix, Fig. 8A) and away from the needle tip (several minutes after it has formed, Appendix, Fig. 8B), the elastic modulus of the filament E can be calculated

from the slope of the linear regime $\frac{2Er^2}{\rho g}$ (Appendix, Fig. 8A and

B). Similarly, this experimental setup was used to compare elastic moduli and effective stiffness of fluid-in-solid composite tubes (Appendix, Fig. 8C). The elastic moduli of the composite tubes were estimated in stretching mode as well, where a filament segment was bent in a 'U' shape and vertically hung from a rigid boundary, and equal weights (metal pins) were placed in the neck of the 'U'. The elastic moduli were then estimated from the slope of the stress (σ)-strain (ε) curves generated from the stretching experiments of the filaments (Fig. 5C, D and Appendix, Fig. 8C, D).

A.2.2 Density of the polymerized composite filaments. For the composite tubes, with inclusions of oil, the effective density of the gelled tubes was estimated as follows. The diameter of the inclusions (n mm) as well as the centre to centre spacing between the inclusions (m mm) were measured from the images (see Fig. 5C). The effective density was then computed

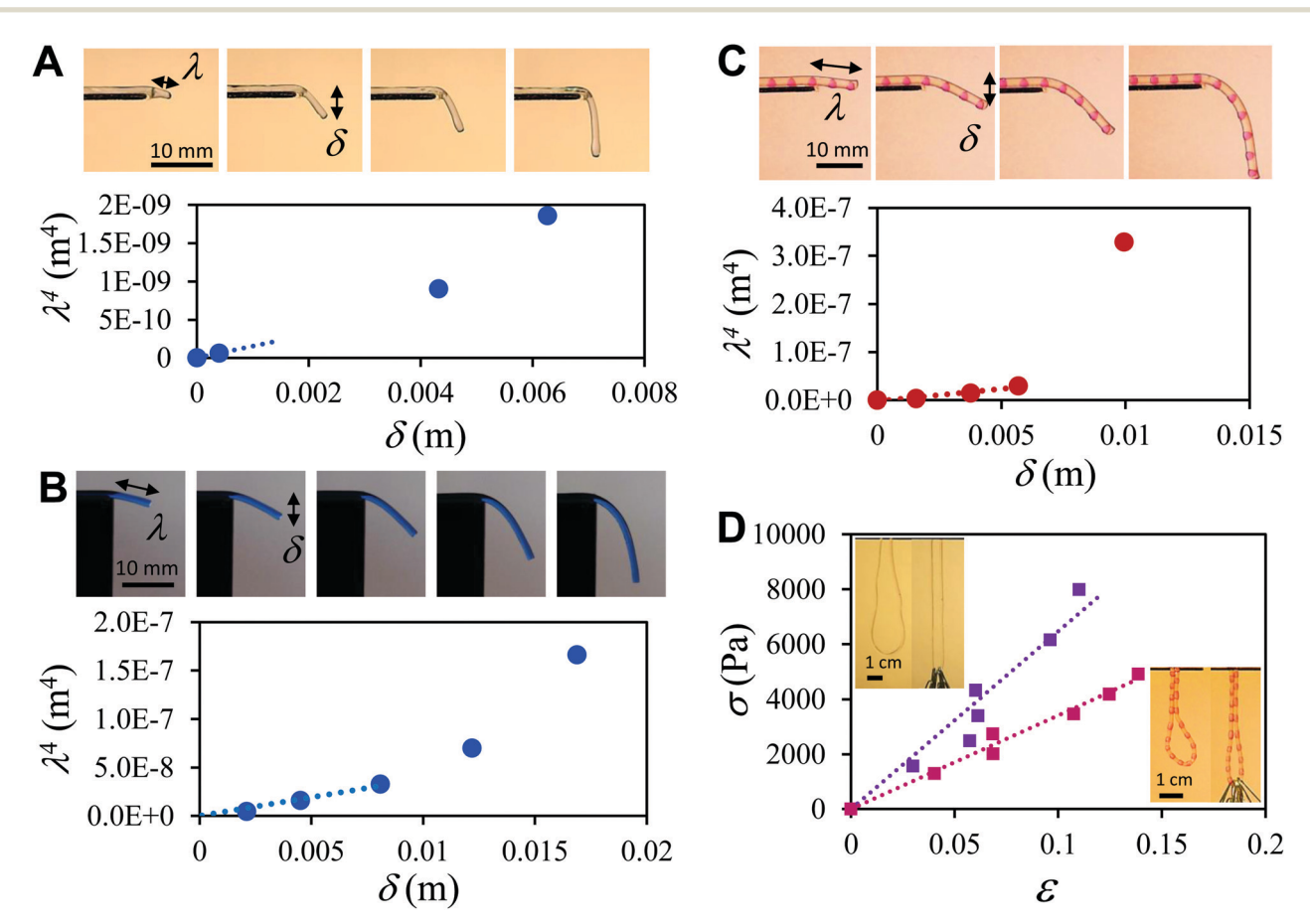


Fig. 8 Direct estimation of bending moduli B and elastic moduli E of pure alginate filaments and composite oil-embedded filaments. (A) Measurement of gravity-induced deflections δ of a crosslinked tube (extracted from the calcium bath seconds after it has formed) of length λ . Plotting λ^4 as a function of δ yields a slope of $2Er^2/pg$ in the linear regime, which gives the elastic modulus E of the alginate tube to be 2.7 kPa. (B) Measurement of λ^4 of a crosslinked tube (extracted from the calcium bath several minutes after it has formed) as a function of δ yields an elastic modulus E of the alginate tube to be 48 kPa. (C) Measurement of gravity-induced deflections δ of a composite tube ($(Q_o - Q_i)/(Q_o + Q_i) = 0.7$, Fig. 5C, filament 3) with silicone oil inclusions to estimate its effective elastic modulus E_c . Plotting λ^4 as a function of δ yields the elastic modulus E_c of the alginate tube to be 36 kPa. (D) Two examples of the stress (σ)-strain (ϵ) curves obtained for measuring elastic moduli of the pure alginate tubes (($(Q_{o}-Q_{i})/(Q_{o}+Q_{i})=1$) and oil-alginate composite tubes $((Q_o - Q_i)/(Q_o + Q_i) = 0.3)$, where $E_{alq} = 71$ kPa (top) and $E_c = 35$ kPa (bottom). The normalized elastic moduli (E_c/E_{alq}) for these two datasets are reported in Fig. 5D.

as $\rho_{\rm eff} = \frac{n}{m} \rho_{\rm oil} + \frac{m-n}{m} \rho_{\rm alg}$, where $\rho_{\rm oil}$ = 972 kg m⁻³ and $\rho_{\rm alg}$ = 1054 kg m⁻³. The size of the inclusions were varied by selecting a needle diameter for the alginate (15G, d = 1.4 mm), then another for the oil (18G, d = 0.84 mm), which were connected via a T-junction, and varying the relative flow rates $(Q_0 - Q_i)$, where Q_0 is the outer alginate flow rate and Q_i is the inner oil flow rate (see Fig. 5A).

A.2.3 Curvature measurement from sections of filaments. The curvature of the filaments could be controlled in the following two ways: (i) by increasing the extrusion flow rate Q_0 , and (ii) by placing fluid inclusions at controlled spacing from the central axes of the tubes. For the first case, the polymerized tubes went from smooth to rough as the flow rate Q_0 increased, while $Q_i = 0$. The curvature in these cases were quantified as shown in Fig. 9. First, threads were held straight from both ends and placed in calcium chloride solution, after which it relaxed into its preferred shape (see Fig. 9B). Then using the ImageJ software, the image is binarized to extract the desired curve, from which the (x, y) coordinates are extracted and calibrated. Finally a moving least square method^{26,27} is used to find a smooth fit of the surface. Once we have a smooth approximation of the curve, we can calculate the curvature of the curve and the corresponding

curvature histogram as shown in Fig. 9C-E. In the second case, nitrogen compressed gas was injected at the source of the extruded polymer tube. If the gas bubble were aligned with the central axis of the gelled tubes, the resulting air-filled tubes were straight. However, as they shifted away from the central axis, the tubes became curved, as quantified in Fig. 5B.

A.3 Simulations

To understand the nonlinear dynamics of the coiling filament, we use a discretized model that involves a set of vertices with positions \mathbf{r}_i (0 $\leq i \leq N+1$) and edges $\mathbf{e}_i \equiv \mathbf{r}_{i+1} - \mathbf{r}_i$ (Fig. 10A), and assume that the discrete filament is inextensible, and that twisting modes equilibrate rapidly relative to bending modes, so that we can effectively ignore them. The bending energy of this discretized model, localized at the vertices, is associated with the change in angle between two neighboring edges

meeting at that vertex, so that the total energy is 28 $\mathscr{E}_b =$

$$\frac{1}{2} \sum_{i=1}^{N} \frac{B}{\Delta l_{i}} \left[2 \tan \left(\frac{\theta_{i}}{2} \right) \right]^{2} \text{ where } l_{i} \equiv |\mathbf{e}_{i}|, \ \hat{\mathbf{t}}_{i} \equiv \mathbf{e}_{i} / l_{i}, \ \Delta l_{i} \equiv (l_{i} + l_{i-1}) / 2$$
 and $\cos \theta_{i} = \hat{\mathbf{t}}_{i} \cdot \hat{\mathbf{t}}_{i-1}$. Then, the force on the *i*th vertex is given by
$$\mathbf{F}_{i}^{b} \equiv -d \mathcal{E}_{b} / d\mathbf{r}_{i}. \tag{A.2}$$

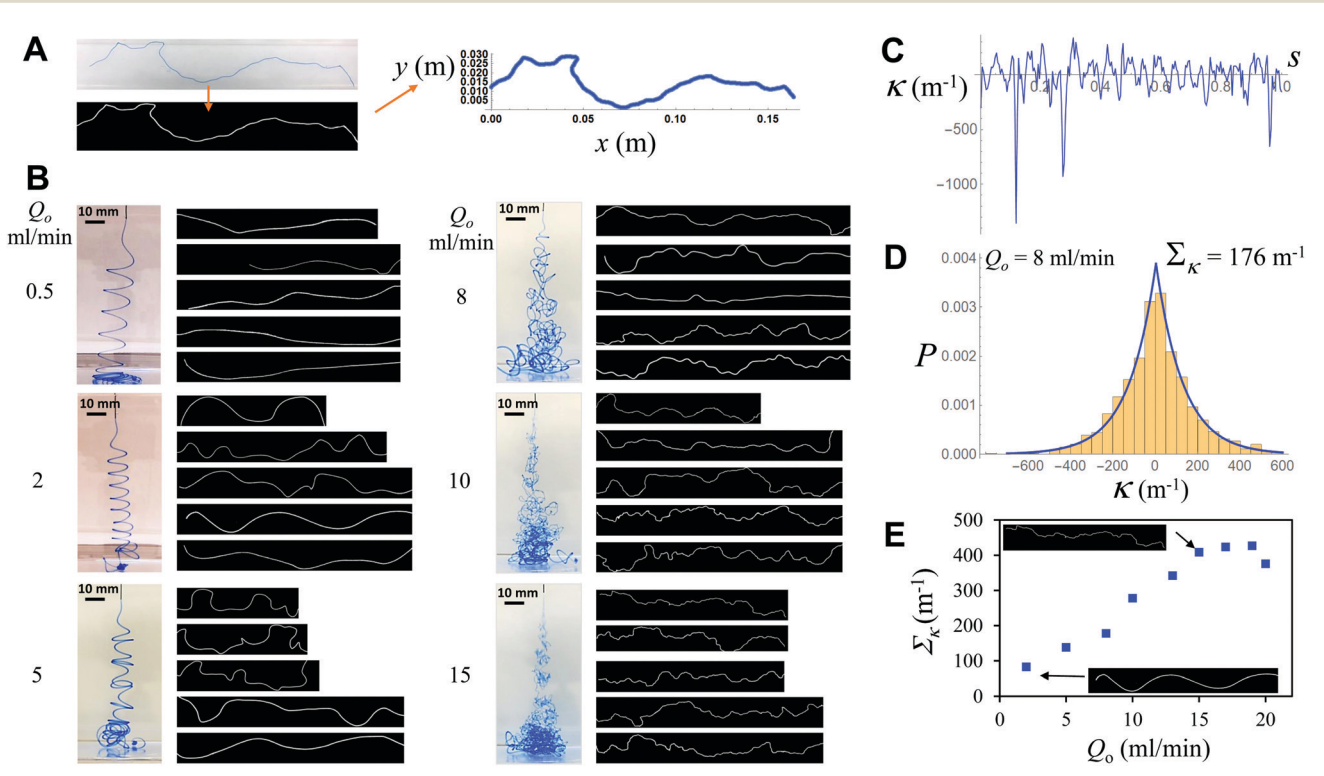


Fig. 9 Estimating the planar curvature of alginate tubes at high extrusion rates: panel (A) shows the sequence of steps performed to obtain a smooth fit to the curves from images. First the image is binarized with pixel values of 1 corresponding to the curve of interest and zero everywhere else. Then, using a calibrated image, the (x, y) Cartesian coordinates of the curve are extracted. Finally a moving least squared approximation is used to obtain a smooth representation of the curve. 26,27 (B) For the needle size 22G (d = 0.41 mm), varying the extrusion rate of the alginate yields smooth gently sinuous tubes at low rates ($Q_o < 8 \text{ ml min}^{-1}$) to rough tubes at higher rates ($Q_o \ge 8 \text{ ml min}^{-1}$). For each Q_o we used 5 examples of the tube segments. (C) Curvature of the filaments from data in (A) as a function of arc length. Panel (D) shows the corresponding curvature histogram, where the curvature values come from multiple samples for the 22G (d = 0.41 mm) needle at $Q_0 = 8$ ml min⁻¹. The blue curve shows the best fitting distribution to the data. (E) Characterization of the chaotic regime via standard deviation of curvature (Σ_k) of the gel tubes formed at high extrusion rates for a specific needle (here 22G, d = 0.41 mm). As Q_o increases, Σ_κ increases and then saturates at very high rates due to the finite thickness of the tubes.

Since the slender filament moves in a viscous liquid at low Reynolds number when inertia is dominated by viscous forces, we use slender-body theory to calculate the drag force¹⁷ which reads

$$\frac{\mathbf{F}_{i}^{\text{drag}}}{\Delta l_{i}} = -\frac{2\pi\mu}{\log(L/r)} \left[2\mathbf{I}_{3} - \hat{\mathbf{t}}_{i}^{\text{T}} \hat{\mathbf{t}}_{i} \right] \left(\mathbf{V}_{i} + \frac{\mathbf{J}_{i}}{\log(L/r)} \right) \\
-\frac{\pi\mu}{\log(L/r)^{2}} \left(2\mathbf{V}_{i}^{\perp} - \mathbf{V}_{i}^{\parallel} \right), \tag{A.3}$$

$$\mathbf{J}_{i} = \mathbf{V}_{i} \log(\Delta l_{i}) + \sum_{j \neq i} \frac{\Delta l_{j}}{2|\mathbf{r}_{i} - \mathbf{r}_{j}|} \times \left[\mathbf{I}_{3} + \frac{(\mathbf{r}_{i} - \mathbf{r}_{j})^{\mathrm{T}}(\mathbf{r}_{i} - \mathbf{r}_{j})}{|\mathbf{r}_{i} - \mathbf{r}_{i}|^{2}}\right] \left[\mathbf{I}_{3} - \frac{1}{2}\hat{\mathbf{t}}_{j}^{\mathrm{T}}\hat{\mathbf{t}}_{j}\right] \mathbf{V}_{j},$$
(A.4)

where $\mathbf{V}_i = d\mathbf{r}_i/dt$ is the velocity of the *i*th vertex relative to the fluid and I_3 is the 3D identity matrix. We note that this is an expansion in inverse powers of log(L/r) and includes the leading nonlocal hydrodynamic interactions which are important for capturing the behavior in our experiments. Finally, each vertex is assumed to have a mass $m_i = \Delta l_i \rho \pi r^2$ so that the velocity, in the unconstrained step, 29 is updated in each time step Δt according to

$$\mathbf{V}_{i}(t + \Delta t) = \mathbf{V}_{i}(t) + \frac{\mathbf{F}_{i}^{b} + \mathbf{F}_{i}^{drag}}{m_{i}} \Delta t.$$
 (A.5)

The inextensibility constraint is implemented numerically using a fast projection method after each time step.²⁹ In order to simulate the extrusion process, we added vertices at the extruding end (inlet point in Fig. 10D-F) at regular time intervals. The vertices are attached elastically to the rest of the rod and provided with an extrusion velocity, and the velocities and positions of all vertices are updated according to (A.5). Implementing this simulation in the C++ code, we first perform a series of checks by comparing the results of the simulation to experiments on sedimenting elastic rods in water, analytical calculations for beam buckling, gravity loading, and the known results for the spool-coiling of a rope falling under gravity onto the ground and get results quantitatively consistent with theory and experiments^{2,3,5} (Fig. 10B-D and Movie S4, ESI†).

To deploy the simulation for a submerged jelling jet, we start with a naturally straight fully crosslinked filament and only keep the first-order (local hydrodynamic interaction) terms in $1/\log(L/r)$ in (A.3) for the viscous drag forces. By using experimentally motivated parameters values (Fig. 10E and Movie S4, ESI†) we find that although the filament starts to coil, over time the coils become disordered in space and unravel in time starting at the bottom free end. The disorder is likely due to the lack of accounting for nonlocal hydrodynamic interactions of the curved filament, while the unraveling is likely due to lack of accounting for cross-linking in our experiments, where the

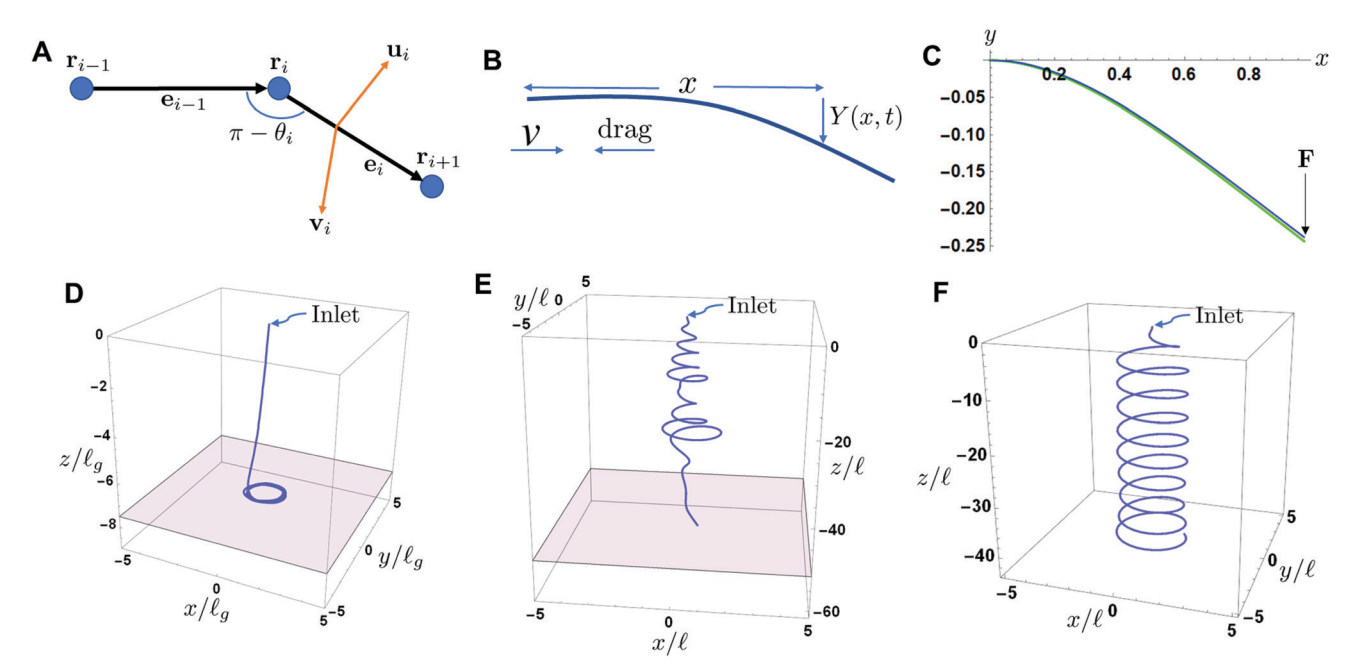


Fig. 10 Numerical simulations of drag induced coiling. (A) The filament is modeled as a discretized rod composed of vertices and edges. \mathbf{r}_i , $0 \le i \le N + 1$ 1, $\mathbf{e}_i = \mathbf{r}_{i+1} - \mathbf{r}_i$ are the edge vectors and θ_i is the angle between two edge vectors meeting at the vertex i. (B) Drag induced instability of a filament with length L and bending stiffness B, moving at a speed v in a bath μ . (C) Beam under tip loading from both simulation and theory. (D) Simulation of a rope falling under gravity onto the ground with no ambient drag. Here $v = 1 \, \mathrm{cm \, s^{-1}}$, $d = 1.5 \, \mathrm{mm}$, $\rho = 1641 \, \mathrm{kg \, m^{-3}}$, $E = 8.5 \, \mathrm{MPa}$ and $\ell_{\mathrm{g}} \equiv (Er^2/\rho g)^{1/3}$. The resulting radius of coiling is consistent with the experiments done in ref. 2 for a drop height of 0.5 m. (E) Simulations of drag induced coiling for a naturally straight, fully crosslinked, rod. Over time the coils produced in the simulation start to unwind due to the lack of forces to maintain the curvature. Parameters used: $E=4.8~\mathrm{kPa},~Q=10~\mathrm{ml~min^{-1}},~d=1~\mathrm{mm},~\Delta\rho=15~\mathrm{kg~m^{-3}}.$ (F) Adding the leading nonlocal hydrodynamic interaction terms (see text) and the effects of slow change in the natural curvature of the filament (see text) in the simulation, leads to regular coiling observed in the experiments (see Movie S4, ESI†). The parameters used are E=2.7 kPa, Q=1 ml min⁻¹, d=0.8 mm, $\Delta \rho=5$ kg m⁻³ and $\mu=0.01$ Pa s.

Paper Soft Matter

curvature of the rod freezes (Fig. 9) and the Young's modulus of the tube material increases over time (Fig. 8A and B), from which we extract the Young's modulus at the time of coiling by requiring that $R \approx 0.4(B/\mu v)^{1/3}$ (Fig. 2B); this yields E = 50 Pa.

To test these hypotheses, we included the second-order terms in $1/\log(L/r)$ and also added the effects of cross linking to the simulation by updating the natural curvature of the rods at each time step in the direction of the actual curvature with a time scale $\tau=1~{\rm s}^{-1}$, corresponding to a slow freezing of the natural curvature even as the filament coils (assumed to follow a simple first-order process). We find that this suffices to capture the experimentally observed behavior associated with regular coiling seen in experiments (Fig. 10F), and compares well with the experimental results shown in Fig. 2 and 6.

Acknowledgements

For partial financial support, we thank the National Science Foundation grants NSF DMR 20-11754, NSF DMREF 19-22321, and NSF EFRI 18-30901.

References

- 1 L. Mahadevan and J. B. Keller, Proc. R. Soc. London, Ser. A, 1996, 452, 1679–1694.
- 2 M. Habibi, N. Ribe and D. Bonn, *Phys. Rev. Lett.*, 2007, **99**, 154302.
- 3 M. K. Jawed, F. Da, J. Joo, E. Grinspun and P. M. Reis, *Proc. Natl. Acad. Sci. U. S. A.*, 2014, **111**, 14663–14668.
- 4 G. I. Taylor, *Proc. Intl. Congress on Theor. Appl. Mechanics*, Springer, 1969, pp. 382-388.
- 5 L. Mahadevan, W. S. Ryu and A. D. Samuel, *Nature*, 1998, 392, 140.
- 6 L. Mahadevan, W. Ryu and A. Samuel, Nature, 2000, 403, 1038.
- 7 N. M. Ribe, J. Fluid Mech., 2017, 812, R2.
- 8 H.-Y. Kim, M. Lee, K. J. Park, S. Kim and L. Mahadevan, *Nano Lett.*, 2010, **10**, 2138–2140.
- 9 P.-T. Brun, C. Inamura, D. Lizardo, G. Franchin, M. Stern, P. Houk and N. Oxman, *Philos. Trans. R. Soc.*, A, 2017, 375, 20160156.

- 10 C. Hu, M. Nakajima, H. Wang, T. Yue, Y. Shen, M. Takeuchi, Q. Huang, M. Seki and T. Fukuda, 2013 13th IEEE International Conference on Nanotechnology (IEEE-NANO 2013), 2013, pp. 529–534.
- 11 P. Dilworth and M. Bogue, *Hand-held three-dimensional drawing device*, US Pat., 9102098, 2015.
- 12 Y.-M. Lin and G. C. Rutledge, *J. Membr. Sci.*, 2018, **563**, 247–258.
- 13 P. Lee and M. Rogers, *Int. J. Gastron. Food Sci.*, 2012, **1**, 96–100.
- 14 K. Machin, J. Exp. Biol., 1958, 35, 796-806.
- 15 F. Gosselin, P. Neetzow and M. Paak, *Phys. Rev. E: Stat.*, *Nonlinear, Soft Matter Phys.*, 2014, **90**, 052718.
- 16 L. Mahadevan and J. B. Keller, SIAM Rev., 1999, 41, 115-131.
- 17 R. G. Cox, J. Fluid Mech., 1970, 44, 791-810.
- 18 G. E. Andrews, R. Askey and R. Roy, *Special functions*, Cambridge University Press, 1999, vol. 71.
- 19 S. Yamani, B. Keshavarz, Y. Raj, T. A. Zaki, G. H. McKinley and I. Bischofberger, *Phys. Rev. Lett.*, 2021, 127, 074501.
- 20 M. A. Skylar-Scott, J. Mueller, C. W. Visser and J. A. Lewis, *Nature*, 2019, 575, 330–335.
- 21 R. W. Style, R. Tutika, J. Y. Kim and M. D. Bartlett, *Adv. Funct. Mater.*, 2021, 31, 2005804.
- 22 M. D. Bartlett and R. W. Style, *Soft Matter*, 2020, **16**, 5799–5800.
- 23 L. Cai, J. Marthelot and P.-T. Brun, *Proc. Natl. Acad. Sci. U. S. A.*, 2019, **116**, 22966–22971.
- 24 H. Onoe, T. Okitsu, A. Itou, M. Kato-Negishi, R. Gojo, D. Kiriya, K. Sato, S. Miura, S. Iwanaga and K. Kuribayashi-Shigetomi, et al., Nat. Mater., 2013, 12, 584–590.
- 25 L. Hu, M. Pasta, F. La Mantia, L. Cui, S. Jeong, H. D. Deshazer, J. W. Choi, S. M. Han and Y. Cui, *Nano Lett.*, 2010, **10**, 708–714.
- 26 R. Kolluri, ACM Transactions on Algorithms (TALG), 2008, 4, 1–25.
- 27 A. Nealen, http://www.nealen.com/projects, 2004, vol. 130, p. 25.
- 28 M. Bergou, M. Wardetzky, S. Robinson, B. Audoly and E. Grinspun, *ACM SIGGRAPH 2008 papers*, 2008, pp. 1–12.
- 29 R. Goldenthal, D. Harmon, R. Fattal, M. Bercovier and E. Grinspun, *ACM SIGGRAPH 2007 papers*, 2007, p. 49.